A soft, adhesive self-healing naked-eye strain/stress visualization patch

Zhi Zhao [a,*], Junjie Liu [b], Mengfei Wu [b], Xuan Yao [a], Haibin Wang [a], Xuemei Liu [a], Zhibin He [c,*], Xiaoyan Song [a,*]

[a] Faculty of Materials and Manufacturing, Key Laboratory of Advanced Functional Materials, Education Ministry of China, Beijing University of Technology, Beijing 100124, China.

[b] Department of Engineering Mechanics, Beijing University of Technology, Beijing, 100124, China.

[c] Department of Vascular Surgery, Peking University People's Hospital, Beijing, 100044, China.

*Corresponding author. E-mail: zhaozhi@bjut.edu.cn, steve_he@sohu.com, xysong@bjut.edu.cn

Abstract

To learn about the strain/stress distribution in a material is essential to achieving its mechanical stability and proper functionality. Conventional techniques such as universal testing machines only applies to static samples with standardized geometry in laboratory environment. Soft mechanical sensors based on stretchable conductors, carbon-filled composites or conductive gels possess better adaptability, but still face challenges from complicated fabrication process, dependence on extra readout device and limited strain/stress mapping ability. Inspired by the camouflage mechanism of cuttlefish and chameleons, here we developed an innovative strain/stress responsive hydrogel containing 'mechano-iridophores'. Force induced reversible phase separation manipulated the dynamic generation of mechano-iridophores, serving as indicators of local deformation. Patch-shaped mechanical sensors made from the responsive hydrogel featured fast response time (<0.4 s), high spatial resolution (~100 μm) and wide dynamic ranges (e.g. 10%-150% strain). The intrinsic adhesiveness and self-healing capability of sensing patches also ensured their excellent applicability and robustness. Importantly, the optical readout allowed strain/stress distributions to

be directly identified by naked eyes or smartphone apps, which had not yet been achieved before. The great advantages above are ideal for developing the next-generation mechanical sensors towards material studies, damage diagnosis, risk prediction and smart devices.

Keywords: strain/stress visualization patch, force responsive hydrogel, biomimicry, self-healing, naked-eye

Introduction

The mechanical behavior of a material plays the key role in its structural stability and proper functionality. As a result, mechanical characterization techniques, especially those that are able to reflect strain and stress changes in real time are being constantly pursued. Conventionally, the strain and stress of a sample is recorded by universal testing machines.[1,2] However, this popular approach has many limitations. The sample needs to be cast into standard shapes in order to obtain accurate results. In addition, universal testing machines are only capable of revealing averaged mechanical parameters of the entire material. Details in local strain/stress state is always missing. Last but not least, the bulky size of the machines makes it almost impossible to conduct on-site measurements in crude environments or probe in-situ mechanical changes in small moving objects.

To overcome the issues above, a variety of soft mechanical sensors (SMS) have been developed during the past decades, which can be directly set onto target samples for in-site measurements. The majority of SMS output electrical signals, whose sensing unit is typically based on stretchable conductors, carbon-filled composites or conductive gels. Stretchable conductors consist of metal nanowire arrays embedded in elastomers. Upon stress, the connection between metal nanowires changes, which induces variations in the electrical resistance.[3-5] Many carbon species, including carbon black, graphene and carbon nanotubes also possess great conductivity. By incorporating

networks of carbon species into elastomers, the as-obtained carbon-filled composites could sense pressure and strain in a way similar to stretchable conductors.[6-8] Conductive gels contain movable ionic species such as ionic liquid, dissolved electrolytes or counterions of the polymer network, which serve as charge carriers. When an external force is applied, the corresponding geometric change of samples and rearrangement of polymers alters the mobility of ionic species, resulting in responses in resistance.[9-11]

In despite of the efforts that have been spent, several limitations still exist in current SMS. First, the fabrication of SMS requires complex multi-step procedures,[12,13] which is costly and less efficient. In addition, the readout of electrical signals highly relies on external devices, making the portability of the entire sensing system not very satisfactory. Finally, the electrical output is scalar and cannot reflect details in spatial distribution of strain/stress. Using an array of SMS may partially solve this problem, but the resolution is greatly limited by the size of individual sensing units, which is at least several millimeters.[3,14] Meanwhile, multiplied sensing units leads to exponentially increased cost and systematic complexity. Therefore, innovative mechanical sensors that can in-situ map strain/stress distributions in a simple and efficient way are greatly desired.

Nature has provided extensive inspirations on environmentally responsive materials. It has been found that iridophores in the dermis of squids and chameleons are able to manipulate their optical properties via structural changes.[15,16] The supramolecular package and geometrical alignment of iridophores is tuned by the state of their proteinaceous components, which leads to tunable light reflection and scattering. Such a mechanism contributes to one of the most precise, heterogeneous appearance controls in living organisms.[17]

Inspired by this, we devised a novel responsive hydrogel system that was able to visualize strain and stress distributions in target material in a biomimetic way. Force induced reversible phase separation yielded ‘mechano-iridophores’, which might be turned on and off to show local strain/stress levels (Figure 1A). Taking advantage of abundant internal carboxyl and amine groups,

the force responsive hydrogels could firmly stick to most substrates, serving as a soft sensing patch featuring fast response speed (<0.4 s), high resolution (~100 μm) and wide dynamic ranges (e.g. 10%-150% strain). The reversible intermolecular interactions also made the sensing patch self-curable and anti-scratching. Importantly, the optical readout of sensing patches could be readily identified by naked eyes, or automatically quantified by smartphones. The great advantages of the sensing patch and the revolutionary sensing strategy provided critical guidance for the development of next-generation SMS.

Materials and methods

Materials

Methacrylic acid (MAAc, 99%), acrylic acid (AAc, 99%), acrylamide (AAm, 99%) and dimethylsulfoxide (DMSO, ≥99.5%) were purchased from Shanghai Macklin Biochemical Co., Ltd. N,N'-methylenebisacrylamide (Bis, 99%), ammonium persulfate (APS, 99.99%), tetramethylethylenediamine (TEMED) and fluorescein O-methacrylate (97%) were purchased from Beijing MREDA Technology Co., Ltd. Pentaethylenehexamine (PEHA, TG) and diethylenetriamine (DETA, 99%) were purchased from Shanghai Aladdin Bio-Chem Technology Co., LTD. N,N,N',N'-tetraethylethylenediamine (TEEED, 98%) was purchased from Shanghai D&B Laboratory Equipment Co., Ltd.

Sample preparation

Force responsive hydrogels were obtained by mixing curable acidic monomers with proper amines, whose molecular structures could be found in Figure S1. Stock solutions were first prepared by dissolving acidic monomers in deionized water (18.2 MΩ/cm). To 1 mL of those stock solutions, a variety of amines were added, followed by the addition of 10 wt.% APS solution to initiate in-situ polymerization. Detailed recipes of all the precursors were listed in Table S1. The typical molar

ratio between acidic monomers and amine molecules in a precursor ranged from 20:1 to 55:1. The reaction mixtures were then cast into various molds and left untouched for a day to form completely cured gels with desired shape. Control samples composed of polyacrylamide were also prepared for comparison purpose. To 1 mL of a 300 mg/mL AAm solution, 10 mg Bis was added, followed by the addition of 100 μL 10 wt.% APS and 0.5 μL TEMED. The precursor was then cast and cured to get desired products.

Characterization of force responsive hydrogels

Microscopic characterizations were carried out on a Leica DM6 microscope. Hydrogel samples were mounted onto a customized extensometer, which controlled the macroscopic strain level of hydrogels. The initial thickness of hydrogel samples was set as 2 mm. To improve the visibility of hydrogels under microscope, fluorescein O-methacrylate was employed to label the samples. Fluorescein O-methacrylate was first dissolved in DMSO to yield a 50 mg/mL stock solution. This solution was then mixed with hydrogel precursors at a 1:100 volume ratio. Due to the presence of methacrylate group, fluorescein O-methacrylate could be incorporated into polymer chains via free radical polymerization following the formula below:

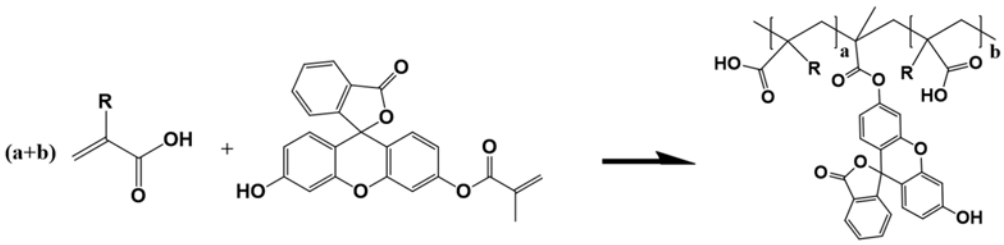

Once the polymers were fluorescent labelled, their structural evolutions could be clearly seen under fluorescent imaging mode. Note the molar ratio between regular monomers and the fluorescent dye was about 6000:1, so introducing the dye had minimal effect on phase separation.

A UV-Vis-NIR spectrometer (FLAME-S-XR1-ES, Ocean Optics) was used to record the transmission spectrum of hydrogel samples. The spectrometer was directly connected to the

microscope (Figure S2). Signals from samples were split by a dichroic mirror, then sent to a CCD camera and the spectrometer to simultaneously record microscopic images and the corresponding spectra.

Infrared (IR) spectra of samples were recorded by a FT-IR spectrometer in the total internal reflection mode (PerkinElmer B420). All samples were sliced into thin layers and completed dried prior to spectral measurements. SEM characterizations were performed with a Nova NanoSEM 200 system. Prior to SEM analysis, all the sample was coated with a ~10 nm layer of gold by a metal evaporator (Bühler Leybold Optics) to improve the electrical conductivity. Tensile tests were performed with an Instron 5948 Micro Tester. The stretching speed was set as 20 mm/min.

Tensile test of hydrogel samples with a pre-crack was conducted on the customized extensometer. The initial dimension of the sample was 12 mm (L) × 6 mm (W) × 2 mm (D). A 3 mm crack was made at the middle of the sample. The sample was then stretched to different strain levels and its pictures were recorded accordingly.

Characterization of the NSV patch

NSV patches were prepared by curing a 2 mm thick hydrogel precursor in a petri dish. After gelation, they were cut into desired shape and applied onto substrates. For adhesion tests, the gel patch was sandwiched between two identical rectangular substrates and gently pressed for 1 min to ensure tight bonding. The contact area between hydrogel and the substrate was maintained at 3 cm × 2 cm by removing excess NSV patch with a razor blade. Six common materials were tested, namely stainless steel (metal), glass, basswood, acrylic board (plastic), cardboard (paper) and nylon elastic belt (fabric). For sensing tests, the patch was covered by a Teflon sheet and then gently pressed against the target substrate for 1 min to ensure tight bonding.

The sensing performance of NSV patches was revealed by stretching and poking tests. The stain in target substrate was shared by NSV patches and reflected by brightness changes. For quantitative

analysis, the brightness of NSV patches under a series of strains was recorded by a camera. ImageJ software was employed to quantify the brightness of NSV patches in the pictures. The relationship between recorded brightness and strain levels was then established to obtain the calibration curve for strain sensing. For stress sensing, tensile curve of target substrate was first measured by an Instron 5948 Micro Tester. The stretching speed was set as 20 mm/min. After that, local strain values could be converted into stress values based on their relationship. A customized app was developed to automatically run the image analysis procedure above on smartphones and output strain/stress distributions in real time.

The self-healing ability of NSV patch was demonstrated by cutting tests. A patch was first cut into halves, and then the two halves were left in contact for 10 min at room temperature. The healed patch was stretched and its responsiveness was evaluated together with pristine patches. The same procedure was also conducted for NSV patches attached to target substrates.

Finite element analysis

Finite element analysis (FEA) on the deformation of hydrogel was implemented with commercial software ABAQUS/Standard. To better reflect experimentally observed results with simulated strain fields, specimens were modeled using the same geometry as that of actual samples, i.e. 12 mm (L) × 6 mm (W) × 2 mm (D) with a pre-crack of 3 mm. The model was set clamped on the bottom and stretched at the top in the direction perpendicular to the crack. To accurately depict the large deformation of the hydrogel, a hyperelastic three-parameter Ogden model was utilized in our simulations, whose parameters were automatically extracted from measured uniaxial quasi-static tensile curve of dog-bone shaped hydrogel samples by ABAQUS. The mesh was defined as four-node plane stress elements (CPS4) with a unified size of 0.3 mm × 0.3 mm, which had been proved to give convergent results.

Software development

Software that automatically quantified the strain and stress distributions within target samples had been developed based on Vue3, echart and Dynamsoft Camera Enhancer. Information on the absolute brightness was directly pulled out from live data collected by smartphone cameras. Prior to the application of external force, the brightness of a designated area was recorded, which served as a reference. Relative brightness was obtained by dividing real-time brightness values by the reference. The relationship between relative brightness and strain/stress levels was typed into the software in advance, which allowed the system to automatically output strain and stress distributions on the screen.

Results and discussions

When an external force was applied onto a material, rearrangement of molecules always happened. The key to visualize strain/stress distributions in a material is finding an effective way to convert local molecular rearrangement into readable optical signals. Previous researches showed that when phase separation happened, transparent hydrogels would turn opaque due to the formation of micron-sized hydrophobic domains, which generated intensive light scattering.[18,19] Nevertheless, phase separation was typically a time-consuming process, which usually took hours to days to complete, let alone its irreversibility under ambient conditions. As a result, it is impractical to employ conventional phase separation for real-time optical sensing.

In previous work, we demonstrated that phase separation with highly tunable structural and mechanical features could be established through a specifically designed molecular system.[20] Briefly, when acrylic acid or its derivative was polymerized with 1,2-diamines, an amine-concentration dependent phase separation happened. The 1,2-diamine unit formed multidentate hydrogen bonding with polyacid chains and served as a physical crosslinker to shorten the distance among hydrophobic groups. Therefore, only if the density of crosslinkers was sufficiently high did hydrophobic interactions took place effectively (Figure S3).

An interesting phenomenon was observed when the amine concentration in the above gel system was slightly below the threshold to trigger phase separation. That is, the hydrogel quickly turned opaque upon the application of external force, and returned to transparent state once the force was released. This force responsive color change originated from a unique strain-assisted phase separation (Figure 1B). When the gel was stretched, for example, the polymer chains became partially aligned along the direction of strain. Consequently, the distance among hydrophobic groups in the perpendicular direction got shortened, reaching the desired level for hydrophobic self-assembly. This effect was essentially equivalent to adding extra amines in terms of facilitating the association of hydrophobic groups. As a result, light-scattering mechano-iridophores (micron-sized hydrophobic domains) emerged under the cooperative effect of multidentate hydrogen bonding and strain induced polymer rearrangement. Once the external force was removed, the configuration of polymer chains got restored so strain-assisted phase separation disappeared. It is worthwhile to note that such force responsive hydrogels were extremely easy to synthesize, which only took a one-step polymerization reaction of proper precursors.

This dynamically reversible phase separation opened up a new strategy to visualize strain/stress in samples (Figure 1B). When the hydrogel tightly attached to a target substrate via various known forms of interfacial interactions,[21] the strain change in the substrate would be faithfully transferred to the hydrogel, rendering visible brightness changes. The flexibility of hydrogel allowed it to fit both plane and curved surfaces. The strain dependent light scattering could be directly told by naked-eyes, serving as a qualitative manner to tell strain distributions. By conducting calibration experiments, it was possible to quantitatively correlate visual color change, strain and stress, which further allowed for automatic strain/stress measurement by software.

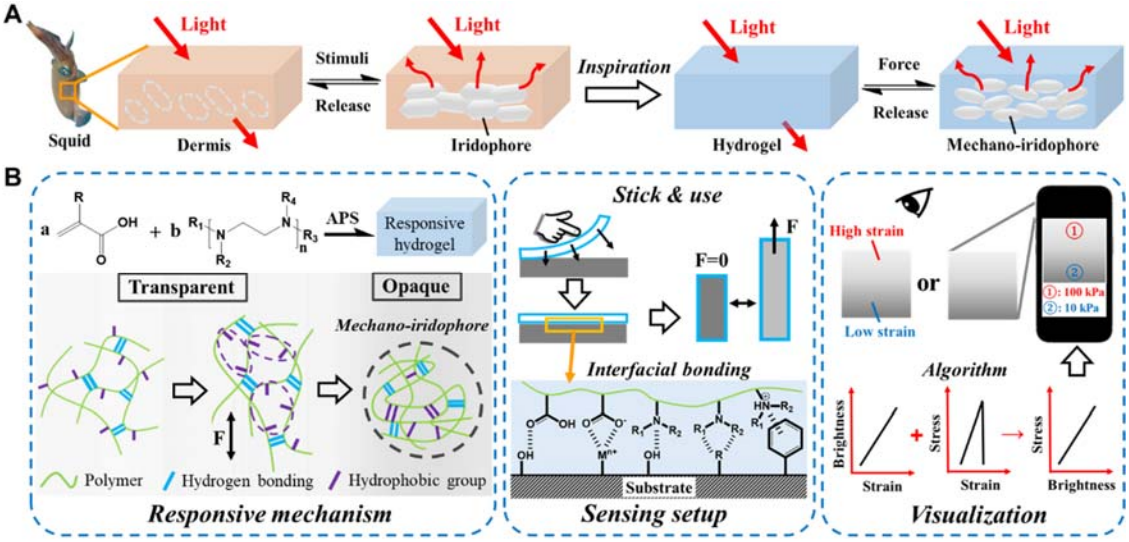

Figure 1. Strain/stress visualization and its applications. (A) Scheme of the bioinspired force responsive hydrogel based on mechano-irridophores. (B) Scheme showing the responsive mechanism, sensing setup and sensing applications of the hydrogel.

The reversible strain-assisted phase separation and formation of mechano-iridophores could be readily confirmed by naked-eyes (Figure 2A). Taking a gel made from AAc and PEHA as an example, the originally transparent hydrogel became white and glistening upon stretching, which turned colorless again after releasing. A video showing the reversible color change can be found in the supplementary information (Video S1). Force triggered microstructure evolution behind the color change was revealed by fluorescent microscopy (Figure 2B-2C). The pristine transparent gel possessed a uniform texture while evenly distributed micron-granules were found in stretched samples. The higher brightness of micron-granules compared with surrounding matrix in the fluorescent image suggested that they contained more densely packed polymers. SEM characterizations further confirmed this discovery (Figure 2D-2E). After being stretched, particulate features showed up in the hydrogel, each of which was about 5-10 μm in diameter. The

geometry and greater substantial density of as-obtained hydrophobic phases was a close mimicry of natural iridophores.

As mentioned above, hydrophobic interactions were the main driven force of strain-assisted phase separation. The presence of associated hydrophobic groups was clearly revealed by FT-IR measurements. It was found that IR bands originated from CH_n groups [22-24] showed obvious difference before and after mechanical deformation. For example, the originally broad C-H deformation bands located at 700-870 cm^{-1} got deconvoluted after stretching. Meanwhile, the C-H bending band at 1272 cm^{-1} became distinguishable in stretched samples (boxed regions in Figure 2F). A similar trend was also discovered for C-H stretching bands (boxed region in Figure 2G). Freshly prepared samples featured a broad IR absorption between 2900-3000 cm^{-1}, which was attributed to overlapped symmetric and asymmetric stretching of CH_2 groups from AAc and PEHA. In comparison, those two modes could be well resolved in stretched samples at 2922 cm^{-1} and 2973 cm^{-1}. The enhanced resolution on the IR bands of CH_n groups indicated that when being stretched, hydrophobic groups aligned in a more regular and confined fashion due to self-assembly (Figure 1B), which reduced the effect of random molecular configuration and local chemical environment on the broadening of their IR absorptions.[25,26]

Notably, the generation of mechano-iridophores had been observed in a series of hydrogels established on the characteristic combination of acrylic acid unit and 1,2-diamine unit (Figure S4A-S4B), demonstrating that such a molecular design could be utilized as a general strategy to realize mechanically regulated hydrophobic self-assembly and biomimetic color switch in hydrogel materials. The uniqueness of this molecular combination lay in its ability to form stable multidentate hydrogen bonding with fixed configuration.[20] In comparison, conventional hydrogels didn't possess the ability to optically indicate local deformation (Figure S4C).

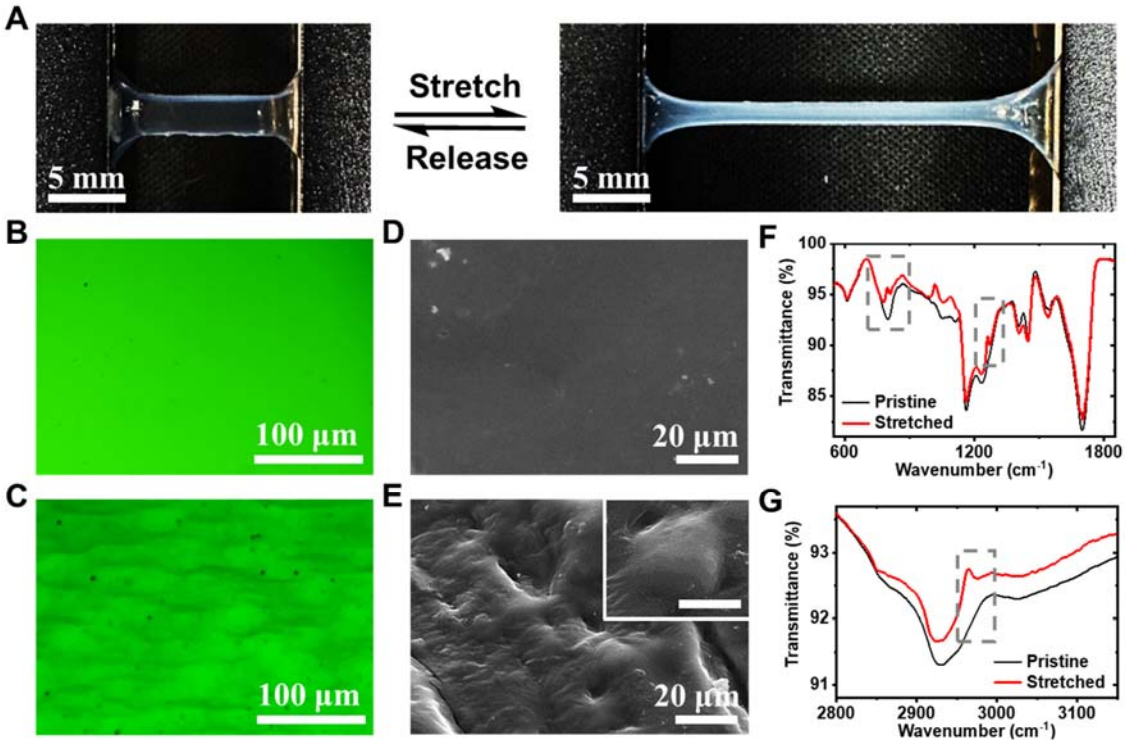

Figure 2. Strain-assisted phase separation and the formation of reversible mechano-iridophores. (A) Strain dependent reversible color change in AAc-PEHA hydrogel (A3). (B) Fluorescent microscopic image of pristine A3 hydrogel. (C) Fluorescent microscopic image of stretched A3 hydrogel. (D) SEM image of pristine A3 hydrogel. (E) SEM image of stretched A3 hydrogel. Inset: a magnified image of an individual machano-iridophore. Scale bar: 5 μm. (F)-(G) IR spectra of pristine and stretch A3 hydrogel.

The degree of phase separation inside force responsive hydrogels above showed an obvious correlation with strain level, which formed the basis to modulate the density of mechano-iridophores and the apparent opaqueness. As the strain level (ε) increased, the hydrogel became darker and darker under microscope due to elevated light blockage by denser iridophores (Figure 3A). The corresponding spectra suggested that when a strain threshold was reached (~10%), the transmission of sample started to drop linearly until reaching a relatively stable level at high ε

(e.g. >150%). The maximum reduction in transmission could reach over 80%. Meanwhile, the reversible formation of iridophores was highly repeatable and dynamically fast. When a sample was subject to cyclic loading and unloading, its transmittance jumped back and forth between two fixed levels at high fidelity (Figure 3B), suggesting the possibility to employ local opaqueness as a reliable quantitative indicator for mechanical deformation levels. The time required to reach the new equilibrium transmittance upon external stimuli was defined as the response time (t_R) of hydrogel samples. A carefully examination showed that the transmittance might be stabilized within as short as 0.4 s after the introduction of stimuli, which was desirable for real time mechanical sensing (Figure 3C). It is worthwhile to mentioned that such a response speed exceeded many previously developed SMS.[27-29]

It is possible to tune the hydrogel's responsiveness to stain though engineering its formula. Details regarding this investigation is included in the supplementary information (Figure S5). As a result, a series of distinctive strain responsive hydrogels could be developed to fit actual demands in real applications.

A great merit of using mechano-iridophores to quantify strains lay in its high-resolution mapping capability. Each iridophore was essentially a 'sensing pixel' that could reveal local change of stains. The micron-size of iridophores allowed them to precisely probe very tiny patterns in strain distributions while the ability to chemically create iridophores at any given spot across the hydrogel made it possible to map strain distributions at macroscopic scale. The ability to map strain had been demonstrated by tensile test of hydrogels with a pre-crack (Figure 3D). Initially, the sample was totally transparent. Upon stretching, the strain was firstly concentrated near the lower tip of the crack (ε=55%). As the overall deformation increased to 90% and 110%, the high-strain regions started to get broadened and shift to the lower part of the sample. The absolute magnitude of local strains also increased, as told by the brighter white color in pictures. When ε reached 130%, the middle of sample underwent obvious neck shrinkage, leading to accumulated strain at the neck and

lower edge. This character of strain distribution would eventually cause the rupture of sample from the bottom.

To verify the accuracy of measured strain distributions, simulations using finite element analysis were conducted. The simulated results well matched experimental observations (Figure 3E). As can be seen, regions with the highest strain concentration in simulations generally showed the brightest color in actual samples. The maximum relative strain at each state increased with the strain level, which was consistent with experimental results. Therefore, mechano-iridophore based force responsive hydrogel was able to directly map strain distributions at high resolution and macroscopic scale without the help of extra devices. To the best of our knowledge, such a capability has not yet been achieved in previous developed SMS.

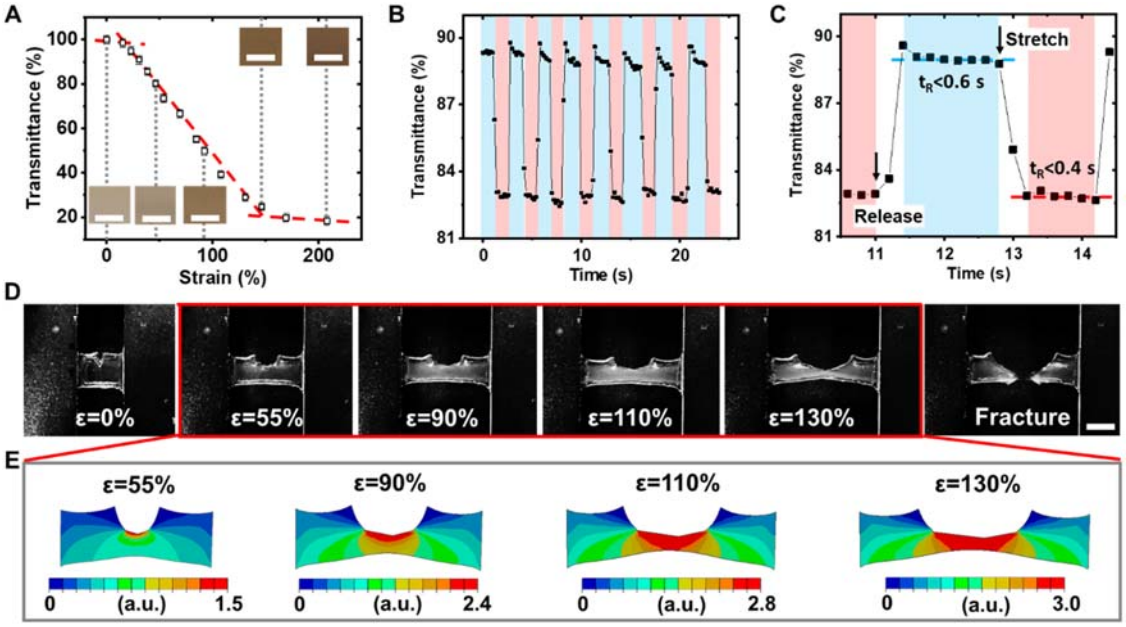

Figure 3. Characteristic properties of the bio-inspired strain responsive hydrogel. (A) Microscopic pictures and transmittance of M2 hydrogel as a function of strain level. Scale bars: 100 μm. (B) Variation in transmittance of M2 hydrogel under cyclic tensile tests. (C) A magnified region in (B) showing the dynamics of strain assisted phase separation. (D) Pictures of a tensile test using M2

hydrogel with a pre-crack. Scale bar: 5 mm. (E) Simulated strain distribution of the sample in (D) under various strain levels. Note the strain level is expressed in relative values.

The characteristic properties of strain responsive hydrogels made them an ideal building block to construct optical sensors for visualizing strain and stress distributions. By casting the hydrogel into flat sheets, naked-eye strain/stress visualization (NSV) patches were prepared, which were then directly applied onto samples of interest for sensing tasks. The soft and flexible nature of NSV patches readily allowed them to fit curved or irregular surfaces. Tensile tests revealed that the mechanical behavior of NSV patches was highly tunable. By engineering the formula of gel precursors, the Young's modulus, tensile strength and fracture strain of NSV patches might be adjusted within a range of 0.07-3.3 MPa, 0.06-2.6 MPa and 700%-3000%, respectively (Figure S6), which could fit different demands in practical applications.

To accurately monitor changes in the strain and stress, it is necessary to establish strong bonding between the NSV patch and target samples so the mechanical deformation in samples could be faithfully transferred to the patch. Interestingly, it had been discovered that NSV patches featured great intrinsic adhesiveness and were able to tightly stick themselves to various substrates. Parallel substrates glued by NSV patches could lift up weights of up to 2.5 kg (Figure 4A). This self-adhesive property was attributed to the abundant carboxyl and amine groups inside the gel. Previous studies suggested that carboxyl and amine groups could effectively interact with a bunch of functional groups on the surface through hydrogen bonding, hydrophobic interactions, cation-π interactions, etc. (Figure 1B), which led to strong interfacial bonding and adhesiveness.[21,30,31]

The adhesion strength of NSV patches to six types of common materials was quantitatively measured. The patch was sandwiched between two pieces of flat substrates and subject to tensile tests (Figure 4B). It was revealed that the adhesion force between NSV patches and the substrates

ranged from 20-180 kPa depending on the material, which was equal to or even greater than that of many classic self-adhesive hydrogels.[32-35] It is worthwhile to mention that a large portion of previously developed SMS were not adhesive themselves.[10,13,36] Therefore, external fixation methods had to be employed, which increased the complexity of sensing procedures. Compare with them, the application of NSV patches could save significant time and labor.

The polymer network in the NSV patch established purely on physical crosslinking, which also provided it with great self-healing abilities. When cracks being introduced, broken multidendate hydrogen bonding could dynamically re-form and connect adjacent polymer chains to repair the wounds. It was found that freshly cut hydrogel pieces could recombine into continuous patch in just a few minutes. The self-healed NSV patch maintained the optical responsiveness to mechanical deformations thereby could still be used in sensing applications (Figure 4C). Notably, concentrated stain was seen at the healed wound upon stretching, indicating that this part should be relatively weaker compared with surrounding areas. This was a common feature in self-healing materials [37,38] and was also properly revealed by the patch. A quick test showed when a NSV patch was scratched, the damaged region was not able to properly indicate local strains (Figure 4D). That is, white lines corresponded to linear cracks on the underlying substrate upon stretching were only detected by intact areas on the patch, but not the wound. After self-healing, the wound was largely fixed. Newly emerged white lines could be observed at the vicinity of the scratch, indicating the sensing ability of this area was recovered (Figure 4E).

The excellent comprehensive performance of NSV patches was summarized and compared with other hydrogels used in mechanical sensing (Figure 4F). Here the working range was defined as the difference between the minimum and maximum value that a sensor could detect, in term of strain (%). The 1 and 0 on self-healing and self-adhesive axis represented ‘yes’ and ‘no’, respectively.

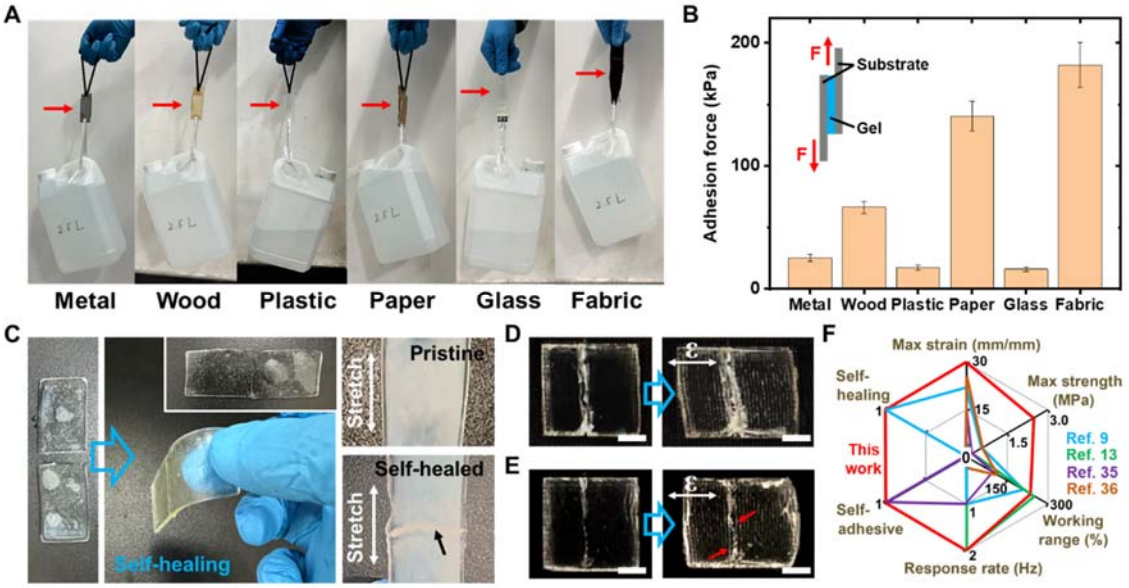

Figure 4. Self-adhesive and self-healing behavior of NSV patches. (A) Pictures showing the adhesiveness of NSV patches by gluing six representative substrates (indicated by arrows). (B) Experimental setup and measured adhesion force of NSV patches on various materials. (C) Self-healing of NSV patches, whose responsiveness to stain remained unaffected. The black arrow pointed to the headed wound. (D) A NSV patch with a scratch and its sensing behavior. Scale bars: 5 mm. (E) Self-healed NSV patch in (D) and its sensing behavior. Red arrows pointed to the newly emerged white lines. Scale bars: 5 mm. (F) A radar plot showing the excellent comprehensive performance of NSV patches.

Taking advantage of the impressive properties of NSV patches, strain/stress distribution of target samples of arbitrary shape could be directly visualized in real time by naked-eyes. A piece of elastic nylon fabric was used as a model for demonstration, which was prone to large in-plane and out-of-plane geometric deformation under external forces. When being stretched in the horizontal direction, white lines perpendicular to the strain appeared, corresponding to periodic linear strain concentrations (Figure 5A). The other areas remained transparent. This type of patterned clearly

evidenced the deformation mechanism. That is, when weft threads were extended under external forces, the shape of warps yarns remained the same. Instead, they widened their gaps to reach the same macroscopic stain. The tiniest linewidth found in the image was below 100 μm, demonstrating the superior spatial resolution of NSV patches in detecting stain distributions. Poking tests were also conducted. Here we chose three random positions on the substrate and sequentially poked them from the back by a pipette tip. Circular while regions corresponded to the three positions were observed following the moving path of pipette tip (Figure 5B). The central part was whiter compared with peripheral regions, indicating that a greater strain presented in the center. In both cases above, the NSV patches quickly turned transparent when external forces were removed (Video S2 and S3). Such a great reversibility was highly desirable in long-term applications.

As a step further, the observed brightness change could be used to quantify local strain/stress levels. To do this, a calibration curve between the brightness of NSV patch and the corresponding strain levels needed to be established first. In order to rule out the effect of environmental light intensity on the optical measurements, relative brightness (B_R) was chosen as a substitution of absolute brightness, which was defined by the following equation:

$$B_R = {B_a}/{B_0}$$

Here B_a and B_0 was the brightness of deformed and original NSV patch recorded under the same conditions, respectively. For demonstration, we used cellphone camera to take pictures of NSV patches from the top, which mimicked the image capturing process of human's eyes. The brightness information was then analyzed by ImageJ software. As can be seen, the B_R value increased linearly with strain levels below ε=100%. After that, the relative brightness reached a plateau, indicating the formation of mechano-iridophores was nearly complete (Figure 5C). With the calibration curve, the strain distributions in a series of target samples could be readily quantified by picturing (Figure 5D). For example, the bright dots appeared on stretched nylon fabric possessed a large strain

concentration (~68%) while the dim lines had relatively low stains (~32%). When being poked, the area located directly on top of the pipette tip featured the largest strain (~62%) while the peripheral regions only had moderate strains (~26%). We had also applied NSV patches onto latex bands. When the bands were extended, the strain was greater at the center and middle edge, and quickly decayed towards left and right ends. The bottom part of the band was intentionally left blank (i.e. without NSV patch) to serve as a control, which proved that the band itself didn't had force responsive optical output.

By conducting tensile tests, the stress-strain relationship of sample materials could be deducted (Figure 5E). Accordingly, the strain distribution might be converted to stress distribution quantitatively (Figure 5F). As can be seen, the high- and low-brightness regions on nylon fabric represented a ~50 kPa difference in stress. The stress at the center/middle edge of a stretched latex band was almost doubled compared with that of other locations. With the data above, it is possible to promptly evaluate whether a risk of rupture exists, and where it will most likely happen.

Once the mechanical property of target material was known, the determination of B_R and its conversion to strain or stress only involved very simple operations. Therefore, it is possible to quickly turn a common cellphone into a powerful mechanical sensor by customized software (Figure S7 and Video S4). With the help of NSV patches, high-resolution, real-time mapping of strain/stress was able to be realized at any place without using specialized equipment.

It is worthwhile to note that stress and strain obtained from tensile measurements were basically averaged values of the entire sample, which might be in discord with the tensile behavior of a specific spot in samples. Consequently, some errors could be introduced into stress distribution characterizations. On the other hand, tensile measurements are currently the standard method to correlate strain and stress. Therefore, further elimination of errors in strain/stress visualization would require conceptual progresses in the field of mechanical characterization, which is out of the scope of this work.

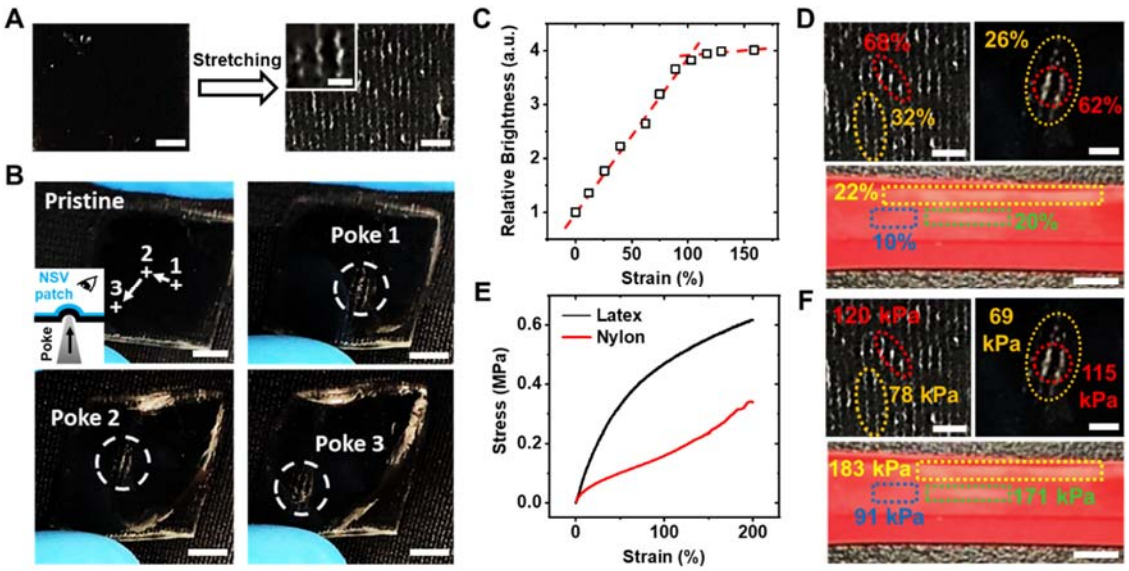

Figure 5. Real time, in-situ strain/stress sensing using NSV patch. (A) Detection of micro-cracks in a fabric. Scale bars: 2 mm. Inset: magnified image of individual white lines. Scale bar: 500 μm. (B) Detection of poking from the back. Scale bars: 5 mm. (C) Stain dependent relative brightness of NSV patches made from recipe A3. (D) Stain distributions in fabric (top) and latex (bottom) samples revealed by NSV patches made from recipe A3. Scale bars: 2 mm (top) and 5 mm (bottom). (E) Tensile curve of the latex and nylon substrate. (F) Stress distributions in fabric (top) and latex (bottom) samples revealed by NSV patches made from recipe A3. Scale bars: 2 mm (top) and 5 mm (bottom).

CONCLUSIONS

In summary, an innovative force responsive hydrogel system had been established based on bioinspired mechano-iridophores. The dynamic generation of mechano-iridophores under external forces led to visible brightness changes, serving as an indicator of local deformation. Patch-shaped mechanical sensors made from such hydrogels featured fast response rate (<0.4 s), high spatial resolution (~100 μm) and wide dynamic ranges (e.g. 10%-150% strain), all of which matched the

best known records. The abundant carboxyl and amine groups offered the gel with great adhesiveness to various substrates while the reversible intermolecular interactions made the gel self-curable and anti-scratching. Importantly, the visible brightness change as a function of strain/stress level could be directly told by naked-eyes and used to characterize strain/stress distributions. Alternatively, such an analytical process might be readily automated using smartphone software, which essentially turned the most common portable device into a powerful mechanical sensor.

To the best of our knowledge, naked-eye optical mechanical sensor simultaneously featured excellent flexibility, response speed, spatial resolution, dynamic range, adhesiveness and self-healing ability had not yet been shown before. The advantages of the presented system made it an ideal candidate for the next generation SMS, which could find broad applications in fundamental material studies, damage diagnosis, risk prediction and smart optical devices.

Supporting Information

Supporting Information is available from the Wiley Online Library or from the author.

Acknowledgements

We would like to thank Mr. Xin Shu and Mr. Yanfeng Wang for their generous help on software development. This work was supported by the National Natural Science Foundation of China (Grant No. 52101032 and 92163107).

Conflict of Interest

The authors declare no conflict of interest.

References

[1] S. Chen, Z. H. Aitken, S. Pattamatta, Z. Wu, Z. G. Yu, D. J. Srolovitz, P. K. Liaw, Y. W. Zhang, *Nat. Commun.* **2021**, *12*, 4953.

[2] Z. Zhao, Y. Shan, H. Wang, H. Lu, X. Liu, B. Wang, X. Song, *Chem. Mater.* **2022**, *34*, 10443.

[3] S. Gong, W. Schwalb, Y. Wang, Y. Chen, Y. Tang, J. Si, B. Shirinzadeh, W. Cheng, *Nat. Commun.* **2014**, *5*, 3132.

[4] M. D. Ho, Y. Ling, L. W. Yap, Y. Wang, D. Dong, Y. Zhao, W. Cheng, *Adv. Funct. Mater.* **2017**, *27*, 1700845.

[5] S. Yao, Y. Zhu, *Nanoscale* **2014**, *6*, 2345.

[6] C. S. Boland, U. Khan, G. Ryan, S. Barwich, R. Charifou, A. Harvey, C. Backes, Z. Li, M. S. Ferreira, M. E. Möbius, R. J. Young, J. N. Coleman, *Science* **2016**, *354*, 1257.

[7] J. Shintake, Y. Piskarev, S. H. Jeong, D. Floreano, *Adv. Mater. Technol.* **2018**, *3*, 1700284.

[8] H. J. Kim, Y. J. Kim, *Mater. Des.* **2018**, *151*, 133.

[9] S. Liu, Y. Qiu, W. Yu, H. Zhang, *ACS Appl. Polym. Mater.* 2020, *2*, 1325.

[10] Q. Wang, Q. Zhang, G. Wang, Y. Wang, X. Ren, G. Gao, *ACS Appl. Mater. Interfaces* **2021**, *14*, 1921.

[11] X. Y. Wang, H. J. Kim, *Prog. Org. Coat.* **2022**, *166*, 106784.

[12] J. Tolvanen, J. Hannu, H. Jantunen, *Sci. Rep.* **2018**, *8*, 13241.

[13] J. Liu, X. Chen, B. Sun, H. Guo, Y. Guo, S. Zhang, R. Tao, Q. Yang, J. Tang, *J. Mater. Chem. A* **2022**, *10*, 25564.

[14] T. Hu, S. Xuan, L. Ding, X. Gong, *Sens. Actuators B Chem.* **2020**, *314*, 128095.

[15] K. M. Cooper, R. T. Hanlon, B. U. Budelmann, *Cell Tissue Res.* **1990**, *259*, 15.

[16] J. Teyssier, S. V. Saenko, D. van der Marel, M. C. Milinkovitch, *Nat. Commun.* **2015**, *6*, 6368.

[17] A. Barbosa, L. M. Mäthger, K. C. Buresch, J. Kelly, C. Chubb, C. C. Chiao, R. T. Hanlon, *Vision Res.* **2008**, *48*, 1242.

[18] T. Nonoyama, Y. W. Lee, K. Ota, K. Fujioka, W. Hong, J. P. Gong, *Adv. Mater.* **2020**, *32*, 1905878.

[19] J. Wu, Z. Zhang, Z. Wu, D. Liu, X. Yang, Y. Wang, X. Jia, X. Xu, P. Jiang, X. Wang, *Adv. Funct. Mater.* **2023**, *33*, 2210395.

[20] Z. Zhao, Y. Li, H. Wang, Y. Shan, X. Liu, M. Wu, X. Zhang, X. Song, *Adv. Sci.* **2023**, 2303315.

[21] C. Y. Shi, D. D. He, Q. Zhang, F. Tong, Z. T. Shi, H. Tian, D. H. Qu, *Natl. Sci. Rev.* **2023**, *10*, nwac139.

[22] J. Zhang, N. A. Peppas, *J. Appl. Polym. Sci.* **2001**, *82*, 1077.

[23] X. Lu, Y. Mi, *Macromolecules* **2005**, *38*, 839.

[24] J. C. Tsai, Y. L. Lo, C. Y. Lin, H. M. Sheu, J. C. Lin, *Spectroscopy* **2004**, *18*, 423.

[25] J. Zhang, H. Tsuji, I. Noda, Y. Ozaki, *Macromolecules* **2004**, *37*, 6433.

[26] M. Zein, R. Winter, *Phys. Chem. Chem. Phys.* **2000**, *2*, 4545.

[27] S. Liu, R. Zheng, S. Chen, Y. Wu, H. Liu, P. Wang, Z. Deng, L. Liu, *J. Mater. Chem. C* **2018**, *6*, 4183.

[28] Z. Wang, J. Chen, L. Wang, G. Gao, Y. Zhou, R. Wang, T. Xu, J. Yin, J. Fu, *J. Mater. Chem. B* **2019**, *7*, 24.

[29] H. Zheng, N. Lin, Y. He, B. Zuo, *ACS Appl. Mater. Interfaces* **2021**, *13*, 40013.

[30] R. Xu, Y. Lai, J. Liu, Q. Wei, W. Sheng, S. Ma, Z. Lei, F. Zhou, *Macromol. Rapid Commun.* **2023**, 2300182.

[31] R. Zhang, H. Ruan, T. Zhou, Q. Fu, H. Peng, X. Zhu, Y. Yao, *Soft Matter* **2019**, *15*, 7381.

[32] L. Wang, Z. Zhao, J. Dong, D. Li, W. Dong, H. Li, Y. Zhou, Q. Liu, B. Deng, *ACS Appl. Mater. Interfaces* **2023**, *15*, 16515.

[33] R. Zhang, H. Ruan, T. Zhou, Q. Fu, H. Peng, X. Zhu, Y. Yao, *Soft Matter* **2019**, *15*, 7381.

[34] H. Zhang, J. He, T. Peng, J. Qu, *ACS Appl. Polym. Mater.* **2022**, *4*, 7575.

[35] F. Mo, Y. Huang, Q. Li, Z. Wang, R. Jiang, W. Gai, C. Zhi, *Adv. Funct. Mater.* **2021**, *31*, 2010830.

[36] Y. Lu, X. Qu, W. Zhao, Y. Ren, W. Si, W. Wang, Q. Wang, W. Huang, X. Dong, *Research* **2020**, *2020*, 2038560.

[37] T. Qin, W. Liao, L. Yu, J. Zhu, M. Wu, Q. Peng, L. Han, H. Zeng, *J. Polym. Sci.* **2022**, *60*, 2607.

[38] V. K. Anupama Devi, R. Shyam, A. Palaniappan, A. K. Jaiswal, T. H. Oh, A. J. Nathanael, *Polymers* **2021**, *13*, 3782.

Supplementary Materials for

A soft, adhesive self-healing naked-eye strain/stress visualization patch

Zhi Zhao*, Junjie Liu, Mengfei Wu, Xuan Yao, Haibin Wang, Xuemei Liu, Zhibin He*, Xiaoyan Song*

Correspondence to: zhaozhi@bjut.edu.cn; steve_he@sohu.com; xysong@bjut.edu.cn

This PDF file includes:

Other Supplementary Materials for this manuscript include the following:

Supplementary Text

Additional facts about strain assisted phase separation in the hydrogel

The key to obtain phase separation is to ensure a close contact among hydrophobic groups. This is usually achieved by introducing abundant crosslinkers. As can be seen, when the amount of TEMED added to 1 mL of precursor changed from 46 μL to 60 μL, the hydrogel partially turned opaque. Further increasing the amount of TEMED led to fully opaque gels (Figure S3A). The color change was caused by the formation of micron-sized light-scattering hydrophobic domains, which was revealed by fluorescent microscopy (Figure S3B).

Alternatively, strain induced polymer rearrangement could also induce phase separation. This effect was observed in several systems containing acrylic acid unit and 1,2-diamine unit (Figure S4A). Micro-granules were observed in the opaque, extended samples (Figure S4B). The uniqueness of this molecular combination lay in its ability to form stable multidentate hydrogen bonding with fixed configuration. Conventional hydrogels didn't contain such groups can rarely reach the same behavior. For example, when common polyacrylamide hydrogel was stretched, its transparency remained unchanged (Figure S4C).

Tuning the responsiveness of force responsive hydrogel

The responsiveness of force responsive hydrogel might be tuned in a rational manner. Assume the threshold of amine concentration to trigger phase separation was C_0, and the actual amine concentration in the hydrogel was C_1. The closer was C_1 to C_0, the more easily strain induced phase separation would happen. This was straightforward to understand since a greater C_1 meant a shorter intrinsic distance among hydrophobic groups. The threshold amine concentration was reached by adding about 70 μL of TEEED in MAAc-TEEED system. Our results indicated that when the

TEEED added to the precursor was 60, 63 and 66 μL, phase separation happened at a strain of 18%, 15% and 10% respectively. Moreover, the decrease of transmittance with strain was much steeper at high amine concentrations. On the other hand, a lower initial content of amine could broaden the dynamic range, which was more suitable for measuring large deformations. For example, the dynamic range of MAAc-TEEED hydrogel with 60, 63 and 66 μL amine was 10%-150%, 15%-180% and 18%-230%, respectively.

Tuning mechanical property of NSV patches

When the concentration of amine groups was maintained at a constant level, the mechanical property of NSV patches was mainly influenced by the type of amine molecules. For hydrophilic acidic monomers like AAc, introducing less hydrophobic amines with a greater number of repeating 1,2-diamine units would lead to better comprehensive mechanical performance (Figure S6A). When hydrophobic substitutional group presented on the acidic monomer (e.g. MAAc), more hydrophobic amines were preferred. Increasing the hydrophobicity of amines resulted in higher tensile strength, but would reduce the elasticity (Figure S6B).

When the structure of reactants was fixed, altering amine concentration was an efficient way to tune the mechanical property (Figure S6C-S6D). In general, a higher amine concentration enhanced the tensile strength while a lower amine concentration led to better elasticity.

By engineering the formula of gel precursors, the Young's modulus, tensile strength and fracture strain of NSV patches might be adjusted within a range of 0.07-3.3 MPa, 0.06-2.6 MPa and 700%-3000%, respectively.

The comprehensive mechanical property of NSV patches was strengthened due to the presence of hydrophobic domains. To demonstrate this, A9 gel was studied as it generated relatively sparse

hydrophobic domains upon deformation, which allowed us to identify finer details under fluorescent microscope. When the gel was stretched in the horizontal direction, many bright lines were observed, which corresponded to the dislocation of polymers (Figure S6E). Interestingly, no dislocation emerged within the hydrophobic domain (pointed by the red arrow). It tended to be deflected and bypass the hydrophobic domain (indicated by the red dashed lines). This indicated that due to the presence of extensive intermolecular interactions, the hydrophobic domain is much tougher than the surrounding matrix. When mechanical deformation happens, it is able to withstand certain levels of external force and keep the structure intact. As long as the hydrophobic domain was not broken apart, it would keep blocking cracking so the complete rupture of material did not happen.

Automated strain and stress quantification by the customized smartphone software

A customized software was developed to quickly quantify strain and stress distribution on smartphone. Video screenshots showing the working process of the software was included in Video S4. Briefly, the strain/stress distribution of NSV patches was first mapped by the software following preset equations. By tapping onto specific spot on the map, the corresponding strain/stress value would be displayed. Results obtained by the software were in consistent with manual measurements (Figure 5D & 5F). For example, nylon fabric being poked from the back featured a circular strain distribution with the highest stain found in the center (Figure S7A). In stretched latex band, a greater stress was found at the middle edge than at the center.

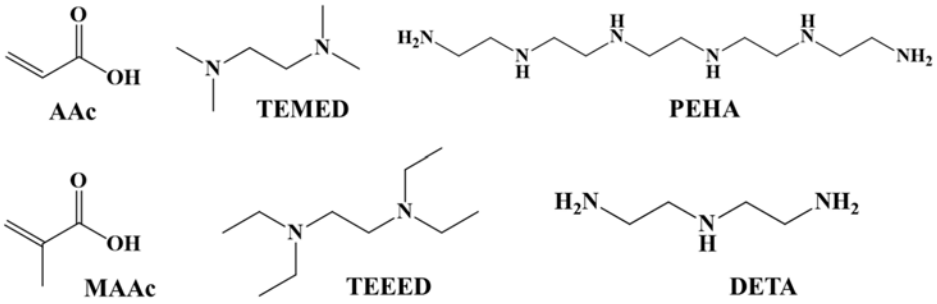

Figure S1. Reactive species used to prepare force responsive hydrogels.

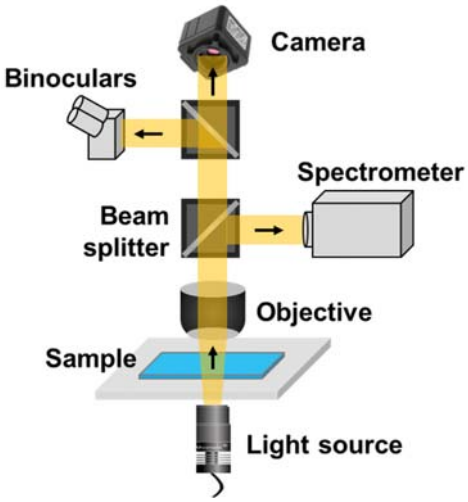

Figure S2. Setup of the spectral microscope.

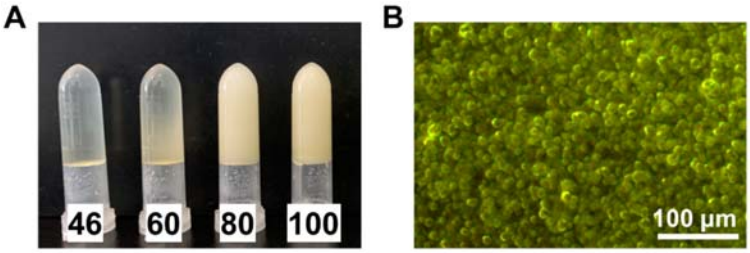

Figure S3. Examples of amine-concentration dependent phase separation. (A) A picture of four AAc-TEMED gels (A5-A8) containing different amount (µL) of TEMED. (B) Fluorescent image showing the granular hydrophobic phases formed in A7 gel.

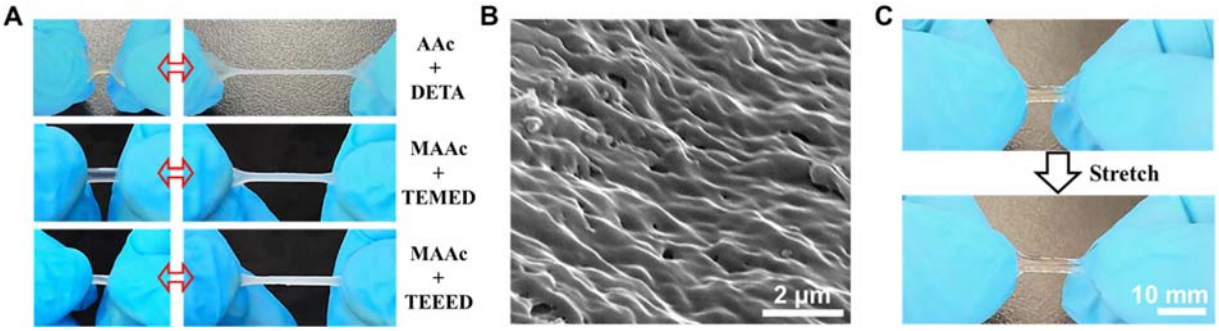

Figure S4. Additional force responsive hydrogels. (A) Additional pictures of force responsive hydrogels (A1, M1 and M4). (B) SEM image of stretched M4 gel. (C) Pictures of polyacrylamide hydrogel in the original and extended state.

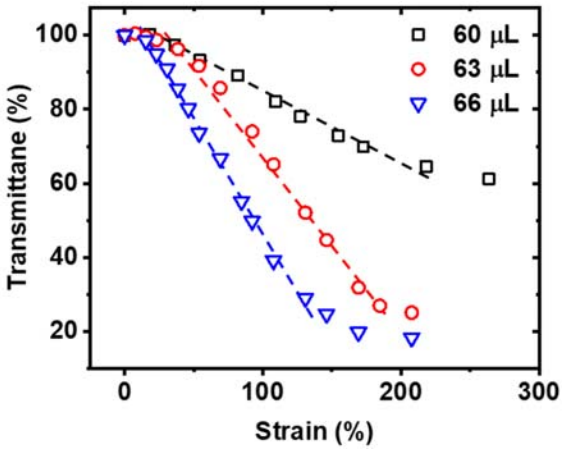

Figure S5. Tunable strain responsive behavior of MAAc-TEEED hydrogels (M2-M4).

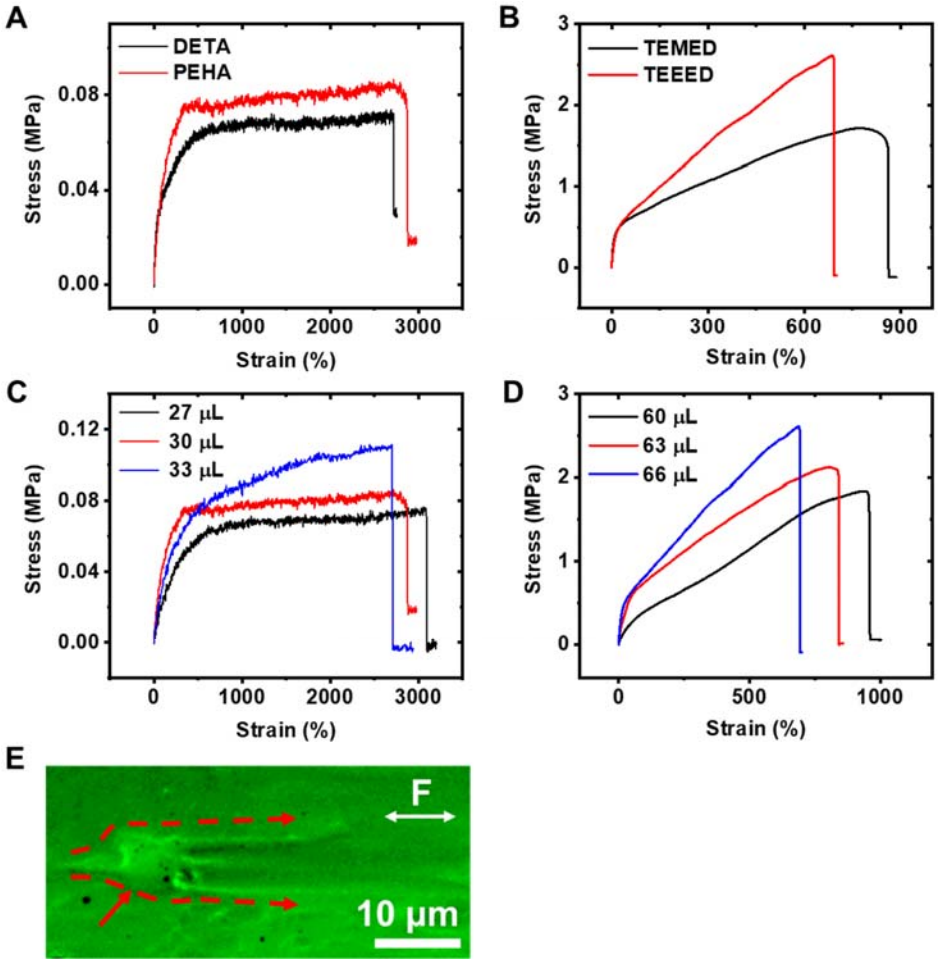

Figure S6. Tunable mechanical properties of NSV patches. (A) The tensile curve of A1 and A4 hydrogel. (B) The tensile curve of M1 and M4 hydrogel. (C) The effect of amine concentration on AAc-PEHA hydrogels (A2-A4). (D) The effect of amine concentration on MAAc-TEEED hydrogels (M2-M4). (E) Fluorescent image of a single hydrophobic domain under external force.

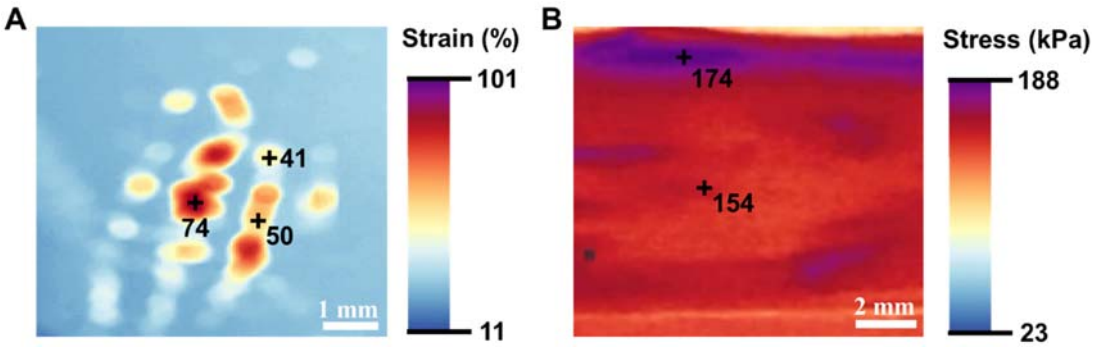

Figure S7. Strain and stress quantification by the customized smartphone software. (A) Automated quantification of strain distribution in a nylon fabric under poking. (B) Automated quantification of stress distribution in a stretched latex band.

Table S1. A list of all the recipes of precursor

Recipe	Hydrgen donor		Hydrogen acceptor		Donor:acceptor ratio	Water (µL)	10 wt% APS (µL)
	Name	Concentration (M)	Name	Volume (µL)			
A1	AAc	6.1	DETA	30	22.4	150	100
A2	AAc	6.1	PEHA	27	55.4	173	100
A3	AAc	6.1	PEHA	30	49.9	170	100
A4	AAc	6.1	PEHA	33	45.3	167	100
A5	AAc	6.1	TEMED	50	18.2	150	100
A6	AAc	6.1	TEMED	60	15.2	140	100
A7	AAc	6.1	TEMED	80	11.4	120	100
A8	AAc	6.1	TEMED	100	9.1	100	100
A9	AAc	3.94	PEHA	25	38.6	175	100
M1	MAAc	6.1	TEMED	46	19.8	140	100
M2	MAAc	6.1	TEEED	60	21.9	140	100
M3	MAAc	6.1	TEEED	63	20.9	137	100
M4	MAAc	6.1	TEEED	66	19.9	134	100

Movie S1.
Force induced reversible color change of an AAc-PEHA hydrogel.

Movie S2.
Strain distribution in a stretched nylon fabric reveal by a NSV patch.

Movie S3.
Strain distribution in a poked nylon fabric reveal by a NSV patch.

Movie S4.
Real time quantification of stain/stress distribution by a cellphone.